Phys. Med. Biol., 1991, Vol. 36, No 8, 1091-1109. Printed in the UK

Ideal versus human observer for long-tailed point spread functions: does deconvolution help?

J P Rolland†, H H Barrett†‡ and G W Seeley†‡§

† University of Arizona, Optical Sciences Center, Tucson, AZ 85721, USA
‡ University of Arizona, Department of Radiology, Health Sciences Center, Tucson, AZ 85724, USA

Received 3 December 1990, in final form 23 April 1991

Abstract. The ideal observer represents a Bayesian approach to performing detection tasks. Since such tasks are frequently used as prototype tasks for radiological imaging systems, the detectability measured at the output of an ideal detector can be used as a figure of merit to characterize the imaging system. For the detectability achieved by the ideal observer to be a good figure of merit, it should predict the ability of the human observer to perform the same detection task. Of great general interest, especially to the medical community, are imaging devices with long-tailed point spread functions (PSFs). Such PSFs may occur due to septal penetration in collimators, veiling glare in image intensifiers or scattered radiation in the body. We have investigated the effect that this type of PSF has on human visual signal detection and whether any improvement in performance can be gained by deconvolving the tails of the PSF. For the ideal observer, it is straightforward to show that the performance is independent of any linear, invertible deconvolution filter. Our psychophysical studies show, however, that performance of the human observer is indeed improved by deconvolution. The ideal observer is, therefore, not a good predictor of human observer performance for detection of a signal imaged through a long-tailed PSF. We offer some explanations for this discrepancy by using some characteristics of the visual process and suggest a standard of comparison for the human observer that takes into account these characteristics. A look at the performance of the non-prewhitening (npw) ideal observer, before and after deconvolution, also brings some good insight into this study.

1. Introduction

The assessment of image quality is a fundamental and ongoing problem in medical imaging. Image quality can be defined by physical measures such as the modulation transfer function, the contrast or the signal-to-noise ratio, but their relation to clinical efficacy is generally unclear. An alternative approach is to consider the performance of the system for some specified tasks. One example is a simple two-hypothesis detection task where we classify a set of images into two categories such as normal and abnormal. The performance of a human observer for the specified task can be measured by psychophysical methods, while the performance of an ideal, Bayesian observer can be calculated using signal detection theory if the parameters of the signal to be detected are known (Green and Swets 1966, Van Trees 1968, Whalen 1971). In either case, performance may be described by a receiver operating characteristic (ROC) curve (Metz 1986). From the area under the ROC curves, indices of detectability may be calculated

§ Deceased.

0031-9155/91/081091+19$03.50

for both the ideal and the human observers. These indices will be referred to as d_{ideal} and d_{human} respectively (Tanner and Birdsall 1958, Goodenough *et al* 1973, Swets and Pickett 1982). The performance of the human observer relative to the ideal observer can then be estimated by computing the human statistical efficiency defined as $(d_{human}/d_{ideal})^2$ (Barlow 1978, Burgess *et al* 1982a).

It is of considerable practical interest to be able to predict the outcome of psychophysical studies, especially if dealing with system design and optimization. The ideal observer is commonly chosen as a standard of comparison for the human observer since, at least for simple tasks, its performance can be readily calculated (Wagner and Brown 1985). To the extent that the performance of the ideal observer correlates well with that of the human, we then have a valuable tool for designing, optimizing and assessing imaging systems. Early studies in this direction were quite promising. For detection of simple, non-random signals in white, Gaussian noise, for example, the ideal observer is a good predictor of human performance (Burgess *et al* 1979, 1981, 1982b, Watson *et al* 1983, Judy *et al* 1987, Legge *et al* 1987, Wagner and Brown 1982). When considering correlated noise, however, human performance can fall far below ideal as suggested by Hanson (1979) and shown convincingly by Myers *et al* (1985). It is therefore important to determine whether there are other practical circumstances where human and ideal performances diverge.

One concrete prediction of the ideal-observer model is that linear filtering of an image cannot improve performance; if filtering is desirable, the ideal observer can do it internally as part of the decision strategy. Thus the question arises whether or not human-observer performance will be improved with linear filtering. Among others, Msaki *et al* (1987), Seibert and Boone (1988), Yanch *et al* (1988) and Fahimi and Macovski (1989) have expended considerable effort in filtering radiographic images to remove scatter. They show that the removal of scattered radiation leads to the enhancement of the contrast in the image. However, in the case of noisy images, both the signal and the noise are enhanced, and it is not clear whether any real improvement is achieved. The intuitive feeling persists, however, that sharper images should somehow be better images. In particular, the authors' intuition suggests that filtering to remove scattering from radiographs should improve their quality, at least for the human observer.

Scattering causes a spread of the PSFs, adding long spatial tails to its compact central core. We refer to such PSF as long-tailed PSFs. Long-tailed PSFs can also arise due to veiling glare in image intensifiers or to septal penetration in nuclear imaging. The main questions addressed in this paper are whether the ideal observer is a good predictor of human performance for systems described by long-tailed PSFs and whether deconvolution is helpful in such cases. Some preliminary results of these studies have already been reported elsewhere (Rolland *et al* 1989a), but a detailed analytic treatment is given in this paper.

To address these questions, two psychophysical studies, described in the next sections as studies I and II, were carried out. Each study was composed of 10 experiments corresponding to different amounts of blur resulting from different spreads of the tail on the PSF. Psychophysical measurements were performed on simulated nuclear medicine images before and after deconvolution. Results of these studies show that the ideal observer greatly overestimates the detection capability of human observers for the assigned task, even when the noise is uncorrelated. They also show that, for our specific detection task, deconvolution does indeed improve the performance of the human observer.

2. Study I: ideal versus human observers before deconvolution

2.1. Theory

The imaging system consists of a radiating object, an image-forming element and a detector. We consider the object to be either a low-contrast signal on a mean background distribution or the background alone. An appropriate example of an image-forming element characterized by a long-tailed PSF is a multibore collimator frequently used for clinical nuclear medicine studies. The long tail in this case results either from scatter in the patient's body or from septal penetration. The detector may be any gamma ray camera such as the familiar Anger camera.

For any given task, one can determine the highest possible detectability by making best possible use of the information in the image. Bayesian theory tells us that this is accomplished by computing the likelihood ratio and comparing it to a threshold; an observer who utilizes this strategy is called ideal. The ideal observer needs to know the object parameters, the PSF and the noise statistics to perform the likelihood test. Our objective here is to assess image quality for a two-hypothesis detection task, where a signal of given width and strength, before being imaged through a long-tailed PSF device, is either present or absent. For each image drawn out of the two classes (signal present or absent), one can compute the likelihood ratio. A useful figure of merit is the signal-to-noise ratio associated with the likelihood ratio, which we shall refer to as the detectability index. We shall derive in this section the expression for the detectability index associated with the ideal observer (d_{ideal}) for the long-tailed PSF case, as well as two other indices, the non-prewhitening (npw) observer (d_{npw}) and the no-low-frequency (nlf) ideal observer (d_{nlf}). The reader who is not interested either in the mathematical derivations of these indices or how the images were simulated (§ 2.2) should skip to § 2.3. (It may be useful, however, to read the paragraph preceding equation (14) to understand the meaning of the nlf observer.)

Let us describe the object, $o(\boldsymbol{r})$, as the superposition of the background, $b(\boldsymbol{r})$, and the signal, $s(\boldsymbol{r})$, where $\boldsymbol{r}$ denotes a two-dimensional (2D) position vector. Both $b(\boldsymbol{r})$ and $s(\boldsymbol{r})$ are precisely known deterministic quantities in this paper; the only randomness is that introduced by the finite number of measured quanta. The overall imaging system may be characterized by a PSF, $p_1(\boldsymbol{r})$, which we take to be the sum of a sharply peaked function, also referred to as the core, $c(\boldsymbol{r})$, of the PSF, and an extended tail $t(\boldsymbol{r})$. The subscript '1' on $p_1(\boldsymbol{r})$ refers to the primary or imaging PSF since we shall introduce later another PSF, $p_2(\boldsymbol{r})$ related to the filtering process. If we call H_0 and H_1 the hypotheses that the signal is absent or present respectively, we can define the mean images $\bar{g}_0(\boldsymbol{r})$ and $\bar{g}_1(\boldsymbol{r})$ under H_0 and H_1 respectively as

$$\bar{g}_0(\boldsymbol{r}) = \kappa T[b*(c+t)](\boldsymbol{r}) \tag{1a}$$

$$\bar{g}_1(\boldsymbol{r}) = \kappa T[(b+s)*(c+t)](\boldsymbol{r}) \tag{1b}$$

where the operator symbol $*$ represents a 2D convolution, κ is an efficiency factor taking into account the geometry of the system, and T is the exposure time (Barrett and Swindell 1981). The actual measured image, $g(\boldsymbol{r})$ can be written as $\bar{g}(\boldsymbol{r}) + n(\boldsymbol{r})$, $n(\boldsymbol{r})$ being the noise of the system and $\bar{g}(\boldsymbol{r})$ the mean count density. Since we are working with digitized images, let us define $g(i) = g(\boldsymbol{r}_i)\varepsilon^2$, $\boldsymbol{r}_i$ being the location of the ith pixel and ε^2 its area. The set of numbers, $g(i)$, defines a vector $\boldsymbol{g}$, and the log-likelihood ratio, l, is given by

$$l = \ln [p(\boldsymbol{g}|H_1)/p(\boldsymbol{g}|H_0)]. \tag{2}$$

The noise is strictly uncorrelated Poisson noise, and the probability densities $p(\boldsymbol{g}|H_k)$, are given by a multivariate Poisson distribution. Because of the uncorrelated nature of Poisson noise, the multivariate probability densities are simply the product over the pixel values of probability densities. If N is the number of pixels, $p(\boldsymbol{g}|H_k)$ can be expressed as

$$p(\boldsymbol{g}|H_k) = \prod_{i=1}^{N} (\bar{g}_k(i)^{g(i)}/g(i)!) \exp(-\bar{g}_k(i)). \tag{3}$$

The log-likelihood ratio given by equation (2) then takes the form

$$l = \sum_{i=1}^{N} g(i) \ln(\bar{g}_1(i)/\bar{g}_0(i) + \text{terms independent of } g(i). \tag{4}$$

In the low-contrast approximation we can write $\bar{g}_1(i) = \bar{g}_0(i) + \Delta\bar{g}(i)$, with $\Delta\bar{g}(i) \ll \bar{g}_0(i)$. If we drop the terms independent of $\boldsymbol{g}$, the expression for l becomes

$$l = \sum_{i=1}^{N} g(i) \ln(1 + \Delta\bar{g}(i)/\bar{g}_0(i)) \simeq \sum_{i=1}^{N} g(i)\, \Delta\bar{g}(i)/\bar{g}_0(i) = (\Delta\bar{\boldsymbol{g}})^{\mathrm{t}} \mathbf{K}_0^{-1} \boldsymbol{g} \tag{5}$$

since for uncorrelated Poisson noise the covariance matrices, $\boldsymbol{K}_k$ $(k = 0, 1)$, are diagonal and, if δ_{ij} is the Kronecker delta function, their elements may be written as

$$\mathbf{K}_k(i, j) = \bar{g}_k(i)\delta_{ij}. \tag{6}$$

Moreover, in the low-contrast approximation, $\mathbf{K}_0 = \mathbf{K}_1 = \mathbf{K}$, and equation (5) becomes

$$l = (\Delta\bar{\boldsymbol{g}})^{\mathrm{t}} \mathbf{K}^{-1} \boldsymbol{g}. \tag{7}$$

Since the covariance matrix, $\mathbf{K}$, is positive definite, $\mathbf{K}^{-1}$ can be factored as $\mathbf{K}^{-1/2}\mathbf{K}^{-1/2}$. Then, if the inverse matrix $\mathbf{K}^{-1}$ exists, $\mathbf{K}^{-1/2}$ also exists, and we can gain more insight into the expression for l by writing equation (7) as

$$l = (\mathbf{K}^{-1/2}\Delta\bar{\boldsymbol{g}})^{\mathrm{t}} (\mathbf{K}^{-1/2}\boldsymbol{g}). \tag{8}$$

This expression for l shows that the data are first filtered by the inverse of the square root of the covariance matrix, an operation known as prewhitening. The ideal Bayesian observer then performs a matched-filtering operation, correlating the prewhitened received data, $\mathbf{K}^{-1/2}\boldsymbol{g}$, with the expected signal, $\Delta\bar{\boldsymbol{g}}$, seen through the prewhitening filter. For this reason this ideal observer is often referred to as the prewhitening matched filter.

A general figure of merit that may be associated with l is the so-called index of detectability, d_{ideal}, defined as

$$d^2_{\text{ideal}} = (\bar{l}_1 - \bar{l}_0)^2/(P_1\sigma_1^2 + P_0\sigma_0^2) \tag{9}$$

where $\bar{l}_k = \langle l|H_k\rangle$, $\sigma_k^2 = \langle (l - \bar{l}_k)^2|H_k\rangle$, with the angle brackets indicating the ensemble average over the elements of the kth class $(k = 0, 1)$, and P_0 and P_1 are the *a priori* probabilities of occurrence of class 0 and 1 respectively, satisfying $P_0 + P_1 = 1$. In the low-contrast approximation, $\sigma_0 = \sigma_1 = \sigma_l$, and the variance reduces to a single term. If we denote $\langle l|H_1\rangle - \langle l|H_0\rangle$ as $\Delta\bar{l}$, then $\Delta\bar{l}$ and σ_l may be calculated from the expression

for the test statistic given by equation (7). The results are

$$\begin{aligned}\Delta\bar{l} &= \langle((\Delta\bar{g})^t\mathbf{K}^{-1}g|H_1\rangle - \langle((\Delta\bar{g})^t\mathbf{K}^{-1}g|H_0\rangle \\ &= (\Delta\bar{g})^t\mathbf{K}^{-1}\langle g|H_1\rangle - (\Delta\bar{g})^t\mathbf{K}^{-1}\langle g|H_0\rangle \\ &= (\Delta\bar{g})^t\mathbf{K}^{-1}\Delta\bar{g} \qquad (10)\end{aligned}$$

$$\begin{aligned}\sigma_l^2 &= \langle((\Delta\bar{g})^t\mathbf{K}^{-1}g - (\Delta\bar{g})^t\mathbf{K}^{-1}\langle g|H_1\rangle)^2|H_1\rangle \\ &= \langle(\Delta\bar{g})^t\mathbf{K}^{-1}(g-\bar{g})(g-\bar{g}_1)^t\mathbf{K}^{-1}\Delta\bar{g}|H_1\rangle \\ &= (\Delta\bar{g})^t\mathbf{K}^{-1}\langle(g-\bar{g}_1)(g-\bar{g}_1)^t|H_1\rangle\mathbf{K}^{-1}\Delta\bar{g} \\ &= (\Delta\bar{g})^t\mathbf{K}^{-1}\mathbf{K}\mathbf{K}^{-1}\Delta\bar{g} \\ &= (\Delta\bar{g})^t\mathbf{K}^{-1}\Delta\bar{g}. \qquad (11)\end{aligned}$$

Equations (10) and (11) show that σ_l^2 equals $\Delta\bar{l}$. This equality results from the low-contrast approximation, which is equivalent here to assuming that the noise is signal independent, though it does depend on the background. Substitution of $\Delta\bar{l}$ and σ_l into equation (9) leads to

$$d^2_{\text{ideal}} = (\Delta\bar{g})^t\mathbf{K}^{-1}\Delta\bar{g}. \qquad (12)$$

The detectability, d_{ideal}, given in a vector form by equation (12), can be expressed explicitly as a function of $s(i)$, $b(i)$, $c(i)$ and $t(i)$ by using equations (1a) and (1b) and noting that $\mathbf{K}^{-1}$ is a diagonal matrix as a result of the uncorrelated nature of the noise. Its non-zero elements are the reciprocals of the noise variances, which are also the mean pixel values according to Poisson statistics. In the approximation of low-contrast signals, the mean values can be calculated by using either equation (1a) or (1b). Equation (12) then becomes

$$d^2_{\text{ideal}} = \kappa T \sum_{i=1}^{N} \frac{[(s*c)(i)+(s*t)(i)]^2}{[(b*c)(i)+(b*t)(i)]}. \qquad (13)$$

Referring to one of the first discoveries on human vision, the brightness-contrast effect, we know that the human observer cannot use an absolute brightness level as a useful piece of information when performing a detection task (Ratliff 1965); instead the human observer is essentially sensitive to contrasts in brightness. When considering the expression of d^2_{ideal} given by equation (13), the term $(s*t)(i)$ appearing in the numerator is a broad, slowly varying component that contains mainly low spatial frequencies. We are going to test the hypothesis that the human observer does not use the information contained in this term when performing the detection task. We define the performance of a pseudo-ideal observer, d_{nlf}, as

$$d^2_{\text{nlf}} = \kappa T \sum_{i=1}^{N} \frac{[(s*c)(i)]^2}{[(b*c)(i)+(b*t)(i)]}. \qquad (14)$$

The denominators in equations (13) and (14) are the same since uncorrelated noise is rich in high spatial frequencies, and the deletion of low frequencies does not significantly affect the noise variance.

Besides evaluating the human observer against the ideal and the nlf ideal observers, we shall also look at the npw ideal-observer predictions for the task at hand. The npw ideal and the ideal observers differ in their ability to take into account noise correlations.

The npw ideal observer, also referred to as the quasi-ideal observer (Wagner and Brown 1985), is a suboptimal observer which assumes uncorrelated and stationary (or 'white') noise. The assumption of uncorrelated noise alone is not sufficient since the noise may be uncorrelated but not stationary, in which case we would not call it white noise. In the case of our experiments where the signal, if present, is superimposed on a Gaussian-shaped background, the statistical process involved should be noted to be non-stationary (see equation (21)). However, since the location of the signal is fixed across the experiments, the noise is indeed locally stationary. The strategy of the npw ideal observer, for performing a discrimination task, is to apply a mask or template on the image in order to perform a cross-correlation of the expected signal with the image data. The test statistic is then given by

$$\lambda = (\Delta\bar{\boldsymbol{g}})^{\mathrm{t}}\boldsymbol{g} \tag{15}$$

where $\Delta\bar{\boldsymbol{g}}$ is the expected signal or template laid on the image data, $\boldsymbol{g}$. The expression for the index of detectability, d_{npw}, is

$$d^2_{\mathrm{npw}} = (\Delta\bar{\lambda})^2/\sigma^2_{\lambda} = ((\Delta\bar{\boldsymbol{g}})^{\mathrm{t}}\Delta\bar{\boldsymbol{g}})^2/(\Delta\boldsymbol{g})^{\mathrm{t}}\mathbf{K}\Delta\boldsymbol{g} \tag{16}$$

where $\mathbf{K}$ is the noise covariance matrix. The expression for d^2_{npw} in terms of $s(i)$, $b(i)$, $c(i)$ and $t(i)$ is then given by

$$\kappa T\left[\sum_{i=1}^{N}[(s*c)(i)+(s*t)(i)]^2\right]^2\left(\sum_{i=1}^{N}[(s*c)(i)+(s*t)(i)]^2[(b*c)(i)+(b*t)(i)]\right)^{-1}. \tag{17}$$

2.2. Image simulations

To investigate the impact that long-tailed PSF have on the detectabilities of the human and the statistical observers, we varied the extent of the tail of the PSF by choosing 10 different widths of the tail of the PSF for a fixed value of the contrast of the core of the PSF relative to the tail. Thus, we generated 10 different sets of images.

Each PSF is expressed as the sum of two Gaussians, as suggested, for example, by Tsui *et al* (1977), to model the core and the tail of the PSF respectively. Their expression is given by

$$p_1(\boldsymbol{r}) = a_{\mathrm{c}}\exp(-r^2/r_{\mathrm{c}}^2) + a_{\mathrm{t}}\exp(-r^2/r_{\mathrm{t}}^2) \tag{18}$$

where a_{c} and a_{t} are the amplitudes of the core and the tail of the PSF respectively, and r_{c} and r_{t} are the half widths at 1/e of the peak intensity of their respective distributions. The width of the core of the PSF is held constant across the 10 sets of images, so that the degradation from one set to the next is essentially due to the broadening of the PSF resulting from adding tails to the core. For the same reason, the contrast of the PSF, defined as $C_{\mathrm{PSF}} = a_{\mathrm{c}}/a_{\mathrm{t}}$, is held constant across the 10 sets of images. The area under the PSF, defined as the integral over the space domain of $p_1(\boldsymbol{r})$, is given by $\pi r_{\mathrm{c}}^2 a_{\mathrm{c}} + \pi r_{\mathrm{t}}^2 a_{\mathrm{t}}$ and is set to 1 (in units of pixels) for normalization purposes. Therefore, given r_{c} and r_{t}, a_{c} and a_{t} can be determined by solving the system of two equations with two unknowns, given by

$$\pi(r_{\mathrm{c}}^2 a_{\mathrm{c}} + r_{\mathrm{t}}^2 a_{\mathrm{t}}) = 1 \tag{19}$$

and

$$a_{\mathrm{c}}/a_{\mathrm{t}} = \mathrm{C}_{\mathrm{PSF}}. \tag{20}$$

For mathematical convenience, we also model the signal $s(\boldsymbol{r})$, and the background, $b(\boldsymbol{r})$ as 2D Gaussian distributions, so that each term in equations (1*a*) and (1*b*) involving a convolution operation takes on a very simple form. The object, $f(\boldsymbol{r})$, is thus described as

$$f(\boldsymbol{r}) = (a_s/\pi r_s^2)\exp(-r^2/r_s^2) + (a_b/\pi r_b^2)\exp(-r^2/r_b^2) \tag{21}$$

where a_s and a_b are now the integrals under the signal and the background distributions, respectively, and r_s and r_b are the half widths at 1/e of the peak intensity of their respective distributions. With such conventions we can expand equation (1*a*) and show that the analytical expression of each of the four terms of the equation is a 2D Gaussian distribution itself. For example, the convolution of the background, $b(\boldsymbol{r})$, with the core of the PSF, $c(\boldsymbol{r})$, yields a 2D Gaussian distribution given by

$$b(\boldsymbol{r}) * c(\boldsymbol{r}) = a_b a_c[r_c^2/(r_b^2 + r_c^2)]\exp[-r^2/(r_b^2 + r_c^2)]. \tag{22}$$

Finally, we define the contrast of the signal on the background to be

$$C_s = (a_s/r_s^2)/(a_b/r_b^2), \tag{23}$$

and given r_s, r_b and C_s, we can solve for a_s and a_b using

$$\kappa T(a_s + a_b) = N_{tot} \tag{24}$$

and

$$a_s/a_b = C_s r_s^2/r_b^2 \tag{25}$$

where N_{tot} is the total number of counts detected. Note that we used the normalization condition given by equation (19) to derive equation (24) and that κ must be in units of reciprocal pixel area for the units on each side of equation (24) to be consistent.

To determine a set of parameters that characterizes the object and the PSF, we assume that the images are sampled on a 128×128-pixel grid. This grid size yields a maximum value for the modulus of the position vector, denoted as r_{max}, of 90.5 pixels. This value constitutes the radius of reference that is used to adjust the widths of the four Gaussian distributions. The width of the background is taken to be the widest, with $r_{max}/r_b = 1$, while the signal is chosen to be 8 pixels in diameter at 1/e of the peak intensity. The core of the PSF is quite sharp, with $r_c = 1.5$ pixels, and the values of r_t, which, are decreasing from set number 1 to set number 10, are such that $r_{max}^2/r_t^2 = N + 2$ where N is the set number. The progression of the extent of the tail of the PSF from set number 1 (PSF_1) to 10 (PSF_{10}) is represented in figure 1. Given the r_t values and a value for C_{PSF}, we can solve equations (19) and (20) for a_t and a_c. The parameters describing the 10 PSFs are given in table 1 for $C_{PSF} = 11$, where the values of r_t are given in pixels and a_c and a_t are dimensionless. The ratio $r_t^2 a_t/r_c^2 a_c$ is a measure of the integral under the tail of the PSF relative to the integral under the core, or the relative strength of the tail with respect to the core of the PSF. The object parameters are adjusted by setting $C_s = 3$ and by adjusting the exposure time such that the noise variance at the peak value of the mean image, denoted as σ_{peak}, is 7% of the peak value, m_{peak}. Moreover, the noise variance is related to the mean pixel value through Poisson statistics, at each point in the image. Thus the noise variance at the peak value of the mean image has to satisfy two conditions:

$$\sigma_{peak} = 0.07\, m_{peak} \tag{26}$$

and

$$\sigma_{peak} = m_{peak}^{1/2} \tag{27}$$

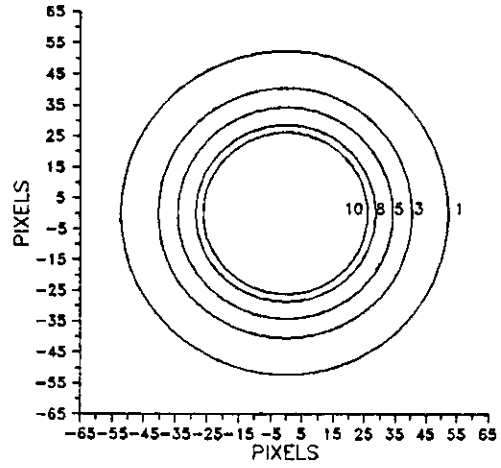

Figure 1. Illustration of the extent of the tail of the PSF from set number 1 to 10. Each circle is centred at the origin of a 128×128 pixel array and has a radius, r_t that satisfies $r_{max}^2/r_t^2 = N+2$, where N is the set number and $r_{max} = 90.5$ pixels.

Table 1. Point spread function parameters: the extent, r_t in units of pixels, of the tail of the PSF, and the amplitudes of the two Gaussians representing the tail and the core of the PSF, a_t and a_c respectively. The parameter α is a measure of the ratio $a_t r_t^2/a_c r_c^2$.

Set number	r_t	a_t	a_c	α
1	52.3	1.1E-03	1.3E-02	110
2	45.3	1.5E-03	1.7E-02	83
3	40.5	1.9E-03	2.1E-02	66
4	37.0	2.3E-03	2.5E-02	55
5	34.2	2.7E-03	2.9E-02	47
6	32.0	3.0E-03	3.3E-02	41
7	30.2	3.4E-03	3.7E-02	37
8	28.6	3.8E-03	4.2E-02	33
9	27.3	4.1E-03	4.6E-02	30
10	26.1	4.5E-03	5.0E-02	28

which yields a value of 204.82 counts/pixel for m_{peak}. For the peak value of the mean image to be 204.82 counts/pixel as we let the PSF vary, the exposure time, or equivalently the total number of counts, N_{tot}, has to be adjusted for each set of images; the resulting values for N_{tot} are given in table 2 along with the corresponding values T for $\kappa = 1$. Note that, while the total number of counts varies from one set of images to the next, the contrast of the signal before imaging is held constant across the 10 sets of images. The contrast of the object after imaging, denoted as C_{is}, ranges from 5.4% corresponding to set number 1 to 17% corresponding to set number 10, as shown in table 2.

We can now compute the performance of the ideal, the nlf and the npw ideal observers by using the values of the PSF and the object parameters given in tables 1 and 2 respectively.

Table 2. Values of the exposure time, T, across the 10 sets of images as well as the total number of counts, N_{tot}. The contrast of the signal after imaging through the 10 PSFs is given by C_{is}.

Set number	T	N_{tot}	C_{is}(%)
1	666	6.7E06	5.4
2	617	6.2E06	6.8
3	584	5.8E06	8.1
4	562	5.6E06	9.4
5	544	5.4E06	10.7
6	529	5.3E06	12.0
7	517	5.2E06	13.3
8	506	5.1E06	14.6
9	496	5.0E06	15.8
10	487	4.9E06	17.1

2.3. Experimental methods

To test the correlation in performance between the ideal and the human observer, 10 psychophysical experiments corresponding to the 10 sets of images were designed. Within each experiment 50 images were generated; 25 images simulated a bright tumour, located in the centre of the image and superimposed on a smooth background, while the tumour was absent in the other 25 images. These two kinds of simulated objects were processed through the image-forming element, $p_1(\boldsymbol{r})$, and uncorrelated Poisson noise was introduced.

The computer-simulated images were displayed using eight bits of available grey levels. They were displayed as 128×128 pixel arrays using the greylevel-to-brightness transfer curve shown in figure 2. One image covered 5.5 cm $\times$ 4.5 cm on the display and each pixel measured 0.43×0.35 mm^2. The light in the room was dimmed down to the same value for all observers. The contrast and brightness levels of the display monitor were fixed during the study and the observers were not allowed to vary them to optimize their performance. Each subject viewed the images binocularly at a

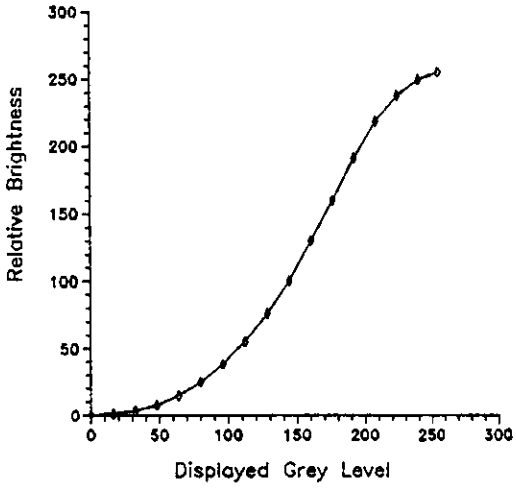

Figure 2. Plot of the measured values of the normalized greylevel-to-brightness transfer curve.

comfortable distance chosen by the observer, and the observers were required to wear their usual correction lenses.

Six observers ran the study, each performing the 10 experiments. The observers first viewed sample images to ascertain the shape, size and location of the object. They did not have any information on the number of occurrences of the signal. The images were displayed in a random order and the 10 experiments were also performed in a randomized order for each observer. On each trial, the observer was presented a single stimulus, either the signal on a noisy background or a noisy background alone. The observer was instructed to rate his certainty on a six-point scale (Green and Swets 1966). From the rating-scale data, an ROC curve was generated for each observer and each experiment (Swets 1979, Swets and Pickett 1982). Five points on a curve were obtained by accumulating data across an observer. All statistics describing the data were derived from non-parametric estimates of the ROC curves generated for each observer and then averaged over all observers (Hanley and McNeil 1982, Metz 1989, Seeley *et al* 1982). We used the estimated value of the area under the ROC curve to compute the detectability index, d_a, referred to as d_{human}. While the use of a single index as a summary of an ROC curve can in some cases lead to misleading data, we did check in our studies that the ROC curves were symmetrical by plotting the ROC themselves and also by checking that the ratio of the variances of the two distributions involved (noise and signal+noise) was approximately unity. This ratio was obtained directly from the output of the ROC analysis on the data.

2.4. Results

The results of the experiments are given in figure 3 where the performance of the human observer versus the ideal and the nlf ideal observers is plotted. We note first that the detectability values achieved by the human observer, which we shall denote as d_{human}, range from 0.4 to 3, which correspond to areas under the ROC curve of 0.610 and 0.983 respectively. The accuracies of the derived indices, d_{human}, though not reported on the graph, were estimated from the sample means and variances of the data. When defined as ratios of standard deviations to the means, the accuracy of d_{human} was found to be approximately 10% for all experiments. A linear regression was performed to fit the experimental data values plotted against the theoretical values. Results show a correlation of the human observer relative to the ideal observer of 0.96 and relative to the nlf ideal observer of 0.98. Despite the high correlation of the data with both figures of merit, figure 3 shows a strong difference in performance between the human observer and the ideal observer. We shall quantify this discrepancy by computing the efficiency in performance of the human observer relative to the two statistical observers.

By analogy with Barlow's definition of statistical efficiency, which is defined as the squared ratio of d_{human} to d_{ideal} and which we shall denote η(ideal), we define a pseudo-efficiency, η(nlf), as the squared ratio of d_{human} to d_{nlf}. The values of η(ideal) and η(nlf) were computed for each experiment by using the experimental and theoretical detectability values (Rolland 1990). Despite the fact that the efficiency values, η(ideal), increased from 0.03 to 0.79% as the tail of the PSF decreased from experiment 1 to 10 respectively, an averaged value over the 10 experiments was calculated since it seems to give some useful measure of human efficiency. We found an average efficiency, η(ideal), of only 0.3% for the human observer with respect to the ideal observer. Moreover, the computation of d_{ideal} and d_{npw} across the 10 experiments yields

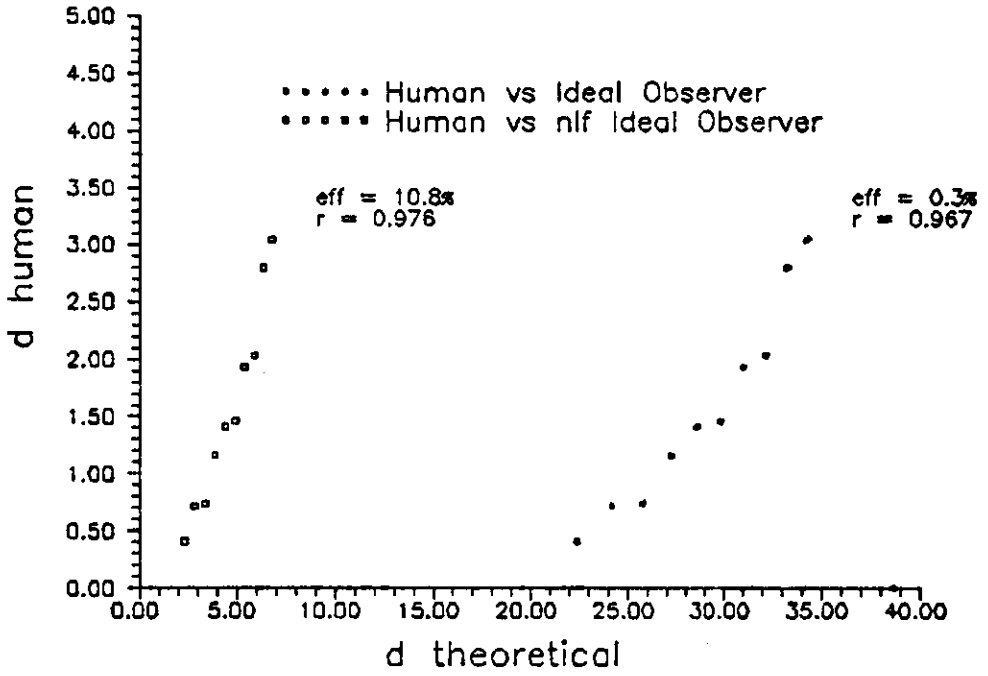

Figure 3. Plot of the detectabilities achieved by the human observer across the 10 experiments, d_{human} (where d_{human} increases from experiment 1 to 10 as the extent of the tail of the PSF decreases) versus the performances of the ideal and the nlf ideal observers referred to as $d_{\text{theoretical}}$ on the graph. The respective values of the correlations, r, and the average (across the 10 experiments) efficiencies, eff, of the human observer with respect to two statistical observers are also given.

about the same values, although the expressions for d_{ideal} and d_{npw} given by equations (13) and (17), respectively are somewhat different. With respect to the nlf ideal observer, results yield an efficiency of the human observer of 10.8% which is a factor of 36 greater than with respect to the ideal observer.

2.5. *Discussion*

Such a low average efficiency value (0.3%) of the human observer relative to the ideal observer across the 10 experiments shows that the ideal observer greatly overestimates the performance of the human observer. This is also the case with the npw ideal observer whose performance in this study is equivalent to that of the ideal observer. The similarity in performance of the ideal and npw ideal observers results from the fact that the noise, although not white, is uncorrelated.

When compared to the nlf ideal observer, the efficiency of the human observer becomes 11%. Such a result seems to indicate that the nlf ideal observer better predicts the performance of the human observer than the ideal observer does.

Since the results of this first study show that the human observer is not using the information present in the image very efficiently, and that the human observer behaves more like the nlf ideal observer, the next step is to try to help the human observer by enhancing the images. We shall thus investigate whether high-pass filtering would be of any help to the human observer. The main question is whether or not the boost and

the correlation in the noise induced by high-pass filtering will nullify the advantage of deconvolution.

3. Study II: human versus statistical observers after deconvolution

3.1. Theory

We want to filter the images to correct for the degradation resulting when the PSF departs from a sharply peaked function. One can invert the convolution process by multiplying the Fourier transform of the image by the reciprocal of the Fourier transform of the PSF, provided this Fourier transform is non-zero over the range of frequencies of interest (Bracewell 1986, Goodman 1988). Such an operation is called deconvolution. If we denote by $\tilde{f}_h(\boldsymbol{\rho})$ the filter used to deconvolve the images, where the subscript h specifies the high-pass nature of the filter, we can design the appropriate filter for each set of images. The general expression for the filters is given by

$$\tilde{f}_h(\boldsymbol{\rho}) = \frac{\tilde{p}_2(\boldsymbol{\rho})}{\tilde{p}_1(\boldsymbol{\rho})} = \frac{(r_c^2 a_c + r_t^2 a_t)\exp(-\pi^2|\boldsymbol{\rho}|^2 r_c^2)}{r_c^2 a_c \exp(-\pi^2|\boldsymbol{\rho}|^2 r_c^2) + r_t^2 a_t \exp(-\pi^2|\boldsymbol{\rho}|^2 r_t^2)} \tag{28}$$

where $\tilde{p}_2(\boldsymbol{\rho})$ is the Fourier transform of the desired zero-tail PSF and $|\boldsymbol{\rho}|$ is the modulus of the 2D frequency vector $\boldsymbol{\rho}$. An inverse Fourier transform is then performed on the filtered images to take us back in the space domain. The nature of the filtering operation is high-pass as shown in figure 4, where an example of the four filters designed to deconvolve the images from set numbers 1, 4, 7 and 10 is given. An example of an image which was presented to the human observers before deconvolution is shown in figure 5 on the left-hand side, while the same image after deconvolution is shown on the right-hand side. While the performances of the ideal and the nlf observers are unchanged with deconvolution, this is not the case for npw ideal-observer performance, which is derived in the Appendix.

The experimental protocol was similar to the study before deconvolution. Each image was displayed using eight bits of greylevels. The images were viewed by the same six observers using the same certainty scale. Sample images were again displayed to the observers to clarify the object parameters and location before the study was run.

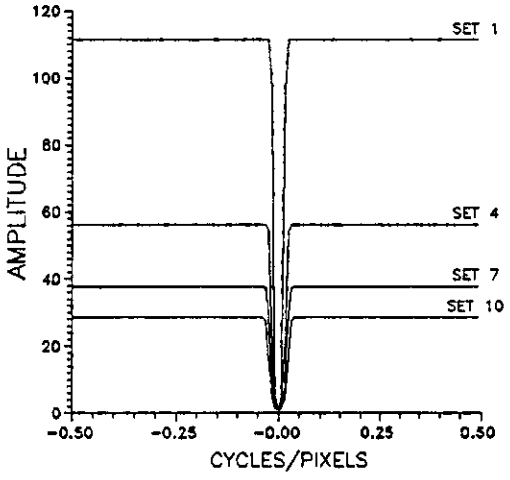

Figure 4. Four examples of the filter used in the Fourier domain to deconvolve the images. Here we show a 1D plot of the shapes of the filters used with the image set numbers 1, 4, 7 and 10. The filters are rotationally symmetric around the zero frequency, where they take the value 1.

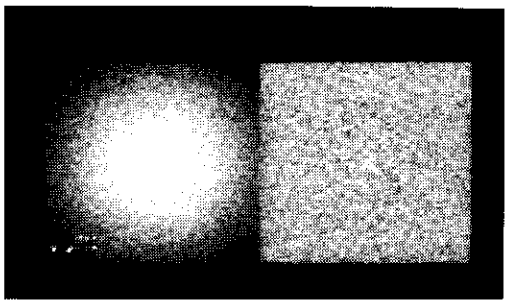

Figure 5. An example of a computer-simulated image before deconvolution on the left-hand side and the same image after deconvolution on the right-hand side.

3.2. Results

The analysis carried out on the data is equivalent to the analysis performed on the data of the previous study. We find that the performance of the human observer has improved due to linear filtering, but is still far below the prediction of the ideal observer, which is invariant under linear filtering. In fact, the efficiency of the human observer with respect to the ideal observer is still as low as 0.6% after deconvolution. Such an efficiency again shows that the ideal observer is a rather poor indicator of human-observer performance for the problem at hand.

A significant increase in performance of the human observer on the deconvolved images relative to the nlf ideal observer across the 10 experiments is shown in figure 6. The average efficiency over the 10 experiments of the human observer with respect to the nlf ideal observer has increased from about 11% before deconvolution to about 20% after deconvolution.

We can also compare this result with the performance that would result from applying a simple matched filter on the deconvolved images. The results show a good prediction of the human-observer performance by the npw ideal observer with a correlation value of 0.99 and an average efficiency of 29%. The performance of the human observer relative to the nlf and the npw ideal observers is graphed in figure 7.

While only the sample mean of the index, d_{human}, is reported on the graphs, its accuracy, as defined previously, was also found to be approximately 10% over the 10 experiments.

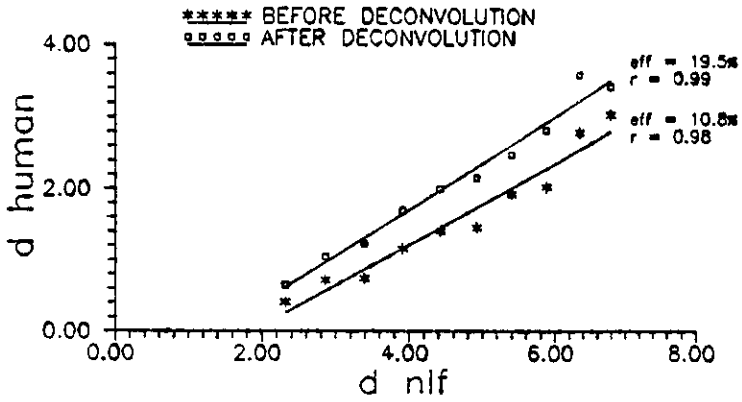

Figure 6. Plot of the detectability values obtained from the psychophysical studies using images before and after deconvolution versus the detectability values predicted by the nlf ideal observer.

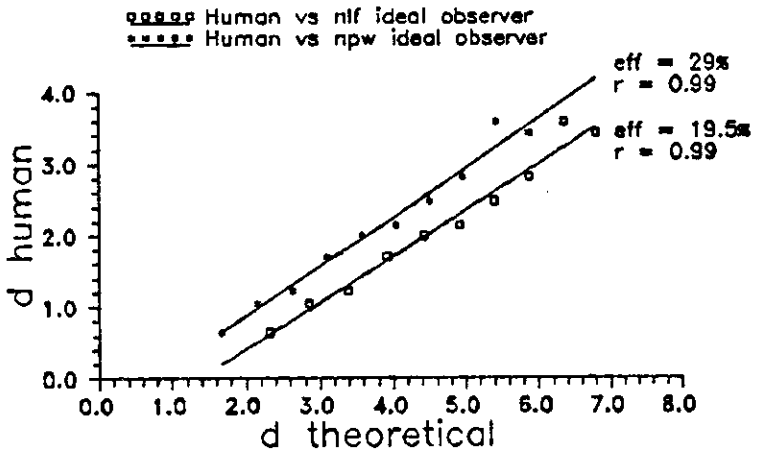

Figure 7. Plot of the detectability values obtained from the psychophysical studies using deconvolved images versus the detectability values predicted by the nlf and npw ideal observers referred to as $d_{\text{theoretical}}$ on the graph.

3.3. Discussion

The low efficiency of the human observer compared to the ideal observer suggests that the ideal observer is not a good predictor of human performance, even after deconvolution. The fact that the ideal observer does not predict human performance after deconvolution is not so surprising if we recall the work of Myers *et al* (1985). They found very low efficiencies for the human observer with respect to the ideal observer when images with negative noise correlations were considered, showing that the human observer is unable to prewhiten the noise. The negative correlations in the noise resulted from filtering the images using high-pass filters, which is similar to our study where we also use the high-pass filters to deconvolve our images. Myers *et al* accepted the npw ideal observer as a better figure of merit to predict human-observer performance. Our results also show a good prediction of human performance using the npw ideal observer after deconvolution, since the npw observer deteriorates markedly after deconvolution and approaches human performance more closely. The effect of deconvolution is to decrease d_{npw}, even though it increases d_{human}. The human appears to be helped because the deconvolution increases the signal strength within the core of the PSF. The npw observer, on the other hand, could make good use of the tails before deconvolution, so clustering the energy into the core does not significantly increase the numerator of the signal-to-noise ratio. The denominator (the noise), on the other hand, is increased by the deconvolution. The net effect is an overall decrease in d_{npw}. We shall note that the npw observer after deconvolution is very similar in concept to the nlf observer although their performances are computed differently.

The increase in performance of the human observer relative to the nlf ideal observer from 11 to 20% reflects the increase in efficiency of the human observer due to deconvolution, since the performance of the nlf ideal observer was computed in either case using equation (14). By construction, the nlf observer was derived to show that the human observer is not making use of the low frequencies; our results show that this is indeed the case. One possible explanation for this increase is that the operation of devonvolution reduces the dynamic range of the images, thus allowing them to be displayed at higher contrast (Burgess 1988). To prove that deconvolution itself does

help the human observer, we investigated the contribution of deconvolution to contrast enhancement apart from the contribution of greyscale mappings. The details of this investigation have already been reported elsewhere (Rolland *et al* 1989b, Rolland 1990), and the main result is that, even without displaying the images using the full scale of available greylevels, deconvolution itself proves to be helpful to the human observer. We also found further improvement in performance after displaying the images using eight bits of available greylevels. This improvement, we believe, can be explained by taking into account the constant internal noise level of the human observer. It was shown very convincingly in a paper by Ishida *et al* (1984) that, although a windowing technique increases both the signal contrast and the image noise by the same factor, the relative magnitude of internal noise with respect to the perceived noise in the image is reduced by image contrast enhancement, and detectability is therefore improved.

4. Conclusion

The study of the impact of long-tailed PSFs on detection of a signal of known location before deconvolution led to the important result that both the ideal observer and the npw ideal observer are poor figures of merit for the problem at hand, the efficiencies taking values of less than 1%. We found that the nlf ideal observer seems to better predict human performance, leading to an average efficiency of 11% over the set of 10 experiments. Such a high discrepancy between the ideal or the npw ideal observers and the nlf ideal observer seems to indicate that the human observer cannot use the signal information encoded in the low-frequency component $(s*t)(\boldsymbol{r})$.

We then showed that linear deconvolution does help the human observer in the detection task, but that the improvement is such that the efficiency of the human relative to the ideal observer increases only from 0.3 to 0.6%. This small increase indicates that the ideal observer is certainly not the appropriate figure of merit to describe the problem of long-tailed PSFs, not only before deconvolution but after deconvolution as well.

We finally showed that, after deconvolution, the human observer yields increased efficiencies when compared to the performance of both the nlf and the npw ideal observers; therefore, under the conditions of this experiment, deconvolution really helps at least the human observer.

Acknowledgments

The authors would like to thank Arthur Burgess, Robert Wagner and Kyle Myers for helpful discussions concerning the interpretation of the data, Mary Ker for her assistance in setting up the psychophysical studies, and all the observers for their patience and cooperation. This work was supported by the national Cancer Institute Grants No P01 CA 23417 and RO1 CA 522643.

Appendix. Derivation of the detectability of the npw ideal observer after deconvolution

If we define as $f_h(\boldsymbol{r})$ the inverse Fourier transform of $\tilde{f}_h(\boldsymbol{\rho})$ given by equation (28) and $\mathbf{F}_h$ the matrix operator associated with $f_h(\boldsymbol{r})$ such that $\boldsymbol{g}^f = \mathbf{F}_h \boldsymbol{g}$, the test statistic after

deconvolution has the form

$$\lambda_{\mathrm{npw}} = \boldsymbol{b}^{\mathrm{t}}\boldsymbol{g}^{\mathrm{f}} \tag{A1}$$

where $\boldsymbol{g}^{\mathrm{f}}$ is the filtered data set and $\boldsymbol{b} = \mathbf{H}\,\Delta f$ with Δf being the difference object under the two hypotheses and $\mathbf{H}_2$ the system operator associated with $p_2(\boldsymbol{r}) = p_1(\boldsymbol{r}) * f_{\mathrm{h}}(\boldsymbol{r})$. We can also write the test statistic as

$$\lambda_{\mathrm{npw}} = \boldsymbol{b}^{\mathrm{t}}\mathbf{F}_{\mathrm{h}}\boldsymbol{g} = \boldsymbol{a}^{\mathrm{t}}\boldsymbol{g} \tag{A2}$$

where $\boldsymbol{a}$ is given by

$$\boldsymbol{a}^{\mathrm{t}} = (\mathbf{H}_2\,\Delta f)^{\mathrm{t}}\mathbf{F}_{\mathrm{h}}. \tag{A3}$$

In the case of our two-hypothesis detection task, Δf is simply the signal s to be detected, and equation (A2) yields

$$\lambda_{\mathrm{npw}} = \boldsymbol{s}^{\mathrm{t}}\mathbf{H}_2^{\mathrm{t}}\mathbf{F}_{\mathrm{h}}\boldsymbol{g}. \tag{A4}$$

The detectability index, d_{npw}, is given by the ratio of $\Delta\bar{\lambda}_{\mathrm{npw}}$ to $\sigma_{\lambda_{\mathrm{npw}}}$, with

$$\begin{aligned}
\Delta\bar{\lambda}_{\mathrm{npw}} &= \langle\lambda_{\mathrm{npw}}|H_2\rangle - \langle\lambda_{\mathrm{npw}}|H_1\rangle \\
&= \boldsymbol{s}^{\mathrm{t}}\mathbf{H}_2^{\mathrm{t}}\mathbf{F}_{\mathrm{h}}(\langle\boldsymbol{g}|H_2\rangle - \langle\boldsymbol{g}|H_1\rangle) \\
&= \boldsymbol{s}^{\mathrm{t}}\mathbf{H}_2^{\mathrm{t}}\mathbf{F}_{\mathrm{h}}\Delta\bar{\boldsymbol{g}} \qquad\qquad (A5)\\
\sigma^2_{\lambda_{\mathrm{npw}}} &= \tfrac{1}{2}[\langle(\lambda_{\mathrm{npw}} - \langle\lambda_{\mathrm{npw}}|H_2\rangle)^2|H_2\rangle + \langle(\lambda_{\mathrm{npw}} - \langle\lambda_{\mathrm{npw}}|H_1\rangle)^2|H_1\rangle] \\
&= \tfrac{1}{2}[\langle[\boldsymbol{s}^{\mathrm{t}}\mathbf{H}_2^{\mathrm{t}}\mathbf{F}_{\mathrm{h}}(\boldsymbol{g} - \bar{\boldsymbol{g}}_2)]^2\rangle + \langle[\boldsymbol{s}^{\mathrm{t}}\mathbf{H}_2^{\mathrm{t}}\mathbf{F}_{\mathrm{h}}(\boldsymbol{g} - \bar{\boldsymbol{g}}_1)]^2\rangle\} \\
&= \tfrac{1}{2}\sum_{k=1}^{2}[\boldsymbol{s}^{\mathrm{t}}\mathbf{H}_2^{\mathrm{t}}\mathbf{F}_{\mathrm{h}}\langle(\boldsymbol{g} - \bar{\boldsymbol{g}}_k)(\boldsymbol{g} - \bar{\boldsymbol{g}}_k)^{\mathrm{t}}\rangle(\mathbf{F}_{\mathrm{h}}^{\mathrm{t}}\mathbf{H}_2\boldsymbol{s})] \\
&= \tfrac{1}{2}\sum_{k=1}^{2}\boldsymbol{s}^{\mathrm{t}}\mathbf{H}_2^{\mathrm{t}}\mathbf{F}_{\mathrm{h}}\mathbf{K}_k\mathbf{F}_{\mathrm{h}}^{\mathrm{t}}\mathbf{H}_2\boldsymbol{s} \qquad\qquad (A6)
\end{aligned}$$

where $\mathbf{K}_k$ is the unfiltered noise covariance matrix for class k. For the case of uncorrelated Poisson noise, and in the low-contrast approximation, equation (A6) yields

$$\sigma^2_{\lambda_{\mathrm{npw}}} = \boldsymbol{s}^{\mathrm{t}}\mathbf{H}_2^{\mathrm{t}}\mathbf{F}_{\mathrm{h}}\mathbf{K}\mathbf{F}_{\mathrm{h}}^{\mathrm{t}}\mathbf{H}_2\boldsymbol{s} \tag{A7}$$

and the detectability index, d_{npw}, becomes

$$\begin{aligned}
d^2_{\mathrm{npw}} &= (\boldsymbol{s}^{\mathrm{t}}\mathbf{H}_2^{\mathrm{t}}\mathbf{F}_{\mathrm{h}}\Delta\bar{\boldsymbol{g}})^2/\boldsymbol{s}^{\mathrm{t}}\mathbf{H}_2^{\mathrm{t}}\mathbf{F}_{\mathrm{h}}\mathbf{K}\mathbf{F}_{\mathrm{h}}^{\mathrm{t}}\mathbf{H}_2\boldsymbol{s} \\
&= \left(\sum_i\sum_j\sum_k s(i)H_2(i,j)F_{\mathrm{h}}(j,k)\Delta\bar{\boldsymbol{g}}(k)\right)^2 \\
&\quad\times\left(\sum_i\sum_j\sum_k\sum_l\sum_m\sum_n s(i)H_2(i,j)F_{\mathrm{h}}(j,k)K(k,l)F_{\mathrm{h}}(l,m)H_2(m,n)s(n)\right)^{-1} \\
&= \left(\sum_i\sum_j\sum_k s(i)H_2(i,j)F_{\mathrm{h}}(j,k)\,\Delta\bar{\boldsymbol{g}}(k)\right)^2\left(\sum_k A(k)\bar{\boldsymbol{g}}_1(k)A(k)\right)^{-1} \\
&= \left(\sum_k A(k)\,\Delta\bar{\boldsymbol{g}}(k)\right)^2\left(\sum_k (A(k))^2\bar{\boldsymbol{g}}_1(k)\right)^{-1} \qquad\qquad (A8)
\end{aligned}$$

where $A(k)$ is given by

$$A(k) = \sum_i\sum_j s(i)H_2(i,j)F_{\mathrm{h}}(j,k). \tag{A9}$$

We can write d_{npw} as a continuous integral in the space domain by taking the limit of the sum when the area of the sampling element tends to zero and by undoing the lexicographic ordering to transform the 1D sums into 2D integrals. The result is

$$d_{\text{npw}}^2 = \left(\int_\infty d^2\boldsymbol{r}\, A(\boldsymbol{r})\, \Delta\bar{g}(\boldsymbol{r}) \right)^2 \left(\int_\infty d^2\boldsymbol{r} (A(\boldsymbol{r}))^2 \bar{g}_1(\boldsymbol{r}) \right)^{-1}$$

$$= [(\Delta\bar{g}(\boldsymbol{r}) * A(\boldsymbol{r}))(0)]^2 / [\bar{g}_1(\boldsymbol{r}) * (A(\boldsymbol{r}))^2](0) \qquad \text{(A10)}$$

where (0) means that the convolution is evaluated at zero shift. Once d_{npw} is expressed as a ratio of convolution operations, it is straightforward to evaluate both the numerator and the denominator in the Fourier domain, a convolution in space domain being transformed into a simple product in Fourier domain.

Résumé

Observateur idéal contre observateur humain pour les fonctions de dispersion ponctuelles présentant une queue de distribution: apport de la déconvolution.

L'observateur idéal représente une approche Bayesienne pour la réalisation des épreuves de détection. Depuis que de telles épreuves sont fréquemment utilisées comme des épreuves prototypes pour les systèmes d'imagerie radiologique, la détectabilité mesurée à la sortie d'un détecteur idéal peut être utilisée comme figure de mérite pour caractériser le système d'imagerie. Pour que la détectabilité évaluée par un observateur idéal présente une bonne figure de mérite, il faut pouvoir évaluer la capacité d'un observateur humain à réaliser la même épreuve de détection. La plupart des systèmes d'imagerie médicale se caractérisent par des fonctions de dispersion ponctuelles (PSFs) présentant des queues de distribution importantes. L'allure des ces PSFs peut être due à la pénétration septale des collimateurs, à la diffusion ('veiling glare') dans les intensificateurs de luminance, ou au rayonnement diffusé par le patient. Les auteurs ont étudié l'effet de ce type de PSF sur la détection d'un signal visuel par un observateur humain afin de voir si une quelconque amélioration pouvait être espérée en réalisant la déconvolution des queues de distribution. Dans le cas d'un observateur idéal, on montre clairement que les performances sont indépendantes d'une déconvolution par filtrage linéaire et réversible. Leurs études psychophysiques montrent cependant que les performances d'un observateur humain sont vraiment améliorées par la déconvolution. L'observateur idéal ne peut pas ainsi être considéré comme un bon indice prédictif des performances d'un observateur humain dans le cas de la détection d'un signal fourni par un système d'imagerie caractérisé par des PSF présentant des queues de distribution. Ils fournissent plusieurs explications à des désaccords, s'appuyant sur quelques caractéristiques du processus visual et suggèrent des normes de comparaison, dans le cas d'un observateur humain, prenant en compte ces caractéristiques. L'observation des performances d'un observateur idéal 'non-prewhitening' (NPW), avant et après déconvolution, donne également un bon aperçu de cette étude.

Zusammenfassung

Idealer Beobachter im Gegensatz zum menschlichen Beobachter bei flach abfallenden Punktbilder: ist Dekonvolution hilfreich?

Der ideale Beonachter bedeutet einen Bayesschen Ansatz zur Durchführung von Nachweisaufgaben. Da solche Aufgaben meist von grundlegender Bedeutung bei radiologischen Abbildungssystemen sind, kann der Grad der Nachweisbarkeit am Ausgang eines idealen Detektors als charakterische Größe des Abbildungssystems verwendet werden. Damit der Grad der Nachweisbarkeit, den ein idealer Beobachter erreicht, der Bedeutung als charakterische Größe gerecht wird, muß die Fähigkeit eines menschlichen Beobachters die gleiche Nachweisaufgabe durchzuführen, vorhergesagt werden können. Von großem allgemeinen Interesse, vor allem im medizinischen Bereich, sind Abbildungssysteme mit flach abfallenden Punktbilder (PSF). Solche PSF können auftreten durch Penetration der Septen von Kollimatoren, durch Überblendung bei Bildverstärkern oder durch Streustrahlung im körper. Untersucht wurde der Einfluß, den die PSF auf das menschliche visuelle Nachweisvermögen hat und ob eine Verbesserung der Leistungsfänigkeit erreicht werden kann durch Dekonvolution des flachen Teils der PSF. Für den idealen Beobachter ist leicht zu zeigen, daß die Leistungsfähigkeit unabhängig ist von jedem linearen, invertierbaren Dekonvolutionsfilter. Psychophysikalische Untersuchungen zeigen jedoch, daß die Leistungsfähigkeit des menschlichen Beobachters

tatsächlich durch Dekonvolution verbessert werden kann. Deshalb ist der ideale Beobachter nicht geeignet zur Vorhersage der Fähigkeit des menschlichen Beobachters zur Feststellung eines Signals, das durch eine flach abfallende PSF abgebildet wird. Diese Unterschiede werden erklärt durch bestimmte Eigenschaften des visuellen Vorgangs und ein Vergleichsstandard wird für den menschlichen Beobachter vorgeschlagen, der diese Eigenschaften berücksichtigt. Die Leistungsfähigkeit des idealen Beobachters, vor und nach der Dekonvolution wird ebenfalls untersucht.

References

Barlow H B 1978 The efficiency of detecting changes in density of random dot patterns *Vision Res.* **18** 637–50

Barrett H H and Swindell W 1981 *Radiological Imaging: The Theory of Image Formation, Detection and Processing* vols I and II (New York: Academic)

Bracewell R N 1986 *The Fourier Transform and its Applications* (New York: McGraw-Hill)

Burgess A E 1988 Personal communications

Burgess A E, Humphrey K and Wagner R F 1979 Detection of bars and discs in quantum noise *SPIE* **173** 34–40

Burgess A E, Jennings R J and Wagner R F 1982a Statistical efficiency: a measure of human visual signal-detection *J Appl. Photo. Eng.* **8** 76–8

Burgess A E, Wagner R F and Jennings R J 1982b Human signal detection performance for noisy medical images *Proc. IEEE ComSoc Int. Workshop on Medical Imaging* (*Asilomar, CA*) IEEE Cat. 82CH1751-7

Burgess A E, Wagner R F, Jennings R J and Barlow H B 1981 Efficiency of human visual discrimination *Science* **214** 93–4

Fahimi H and Macovski A 1989 Reducing the effects of scattered photons in x-ray projection imaging *IEEE Trans. Med. Imag.* **MI8** 56–63

Goodenough D J, Metz C E and Lusted L B 1973 Caveat on the use of the parameter d' for evaluation of observer performance *Radiology* **106** 565–6

Goodman J W 1988 *Introduction to Fourier Optics* (New York: McGraw-Hill)

Green D B and Swets J A 1966 *Signal Detection Theory and Psychophysics* (New York: Wiley) (reprints with corrections: New York: Huntington, 1974)

Hanley J A and McNeil B J 1982 The meaning and use of the area under a receiver operating characteristic (ROC) curve *Radiology* **143** 29–36

Hanson K M 1979 Detectability in computed tomographic images *Med. Phys.* **6** 441–51

Ishida M, Doi K, Loo L L, Metz C E and Lehr J L 1984 Digital image processing: effect on detectability of simulated low-contrast radiographic patterns *Radiology* **150** 569–75

Judy P F and Swensson R G 1987 Display thresholding of images and observer detection performance *J. Opt. Soc. Am.* **A4** 954–65

Legge G E, Kersten D and Burgess A E 1987 Contrast discrimination in noise *J. Opt. Soc. Am.* **A4** 391–404

Metz C E 1986 ROC methodology in radiologic imaging *Invest Radiol.* **21** 720–33

—— 1989 Some practical issues of experimental design and data analysis in radiological studies *Invest. Radiol.* **24** 234–45

Msaki P, Axelsson B, Dahl C M and Larsson S A 1987 Generalized scatter correction method in SPECT using point scatter distribution functions *J. Nucl. Med.* **26** 1861–9

Myers K J, Barett H H, Borgstrom M C, Patton D D and Seeley G W 1985 Effect of noise correlation on detectability of disk signals in medical imaging *J. Opt. Soc. Am.* **A2** 1752–9

Ratliff F 1965 *Mach Bands* (San Francisco: Holden Day)

Rolland J P 1990 Factors influencing lesion detection in Medical imaging *PhD dissertation*

Rolland J P, Barrett H H and Seeley G W 1989a Psychophysical study of deconvolution for long-tailed point-spread functions *The Formation Handling and Evaluation of Medical Images* ed M A Viergever and Todd-Pokropek NATO ASI Series

—— 1989b Quantitative study of deconvolution and display mappings for long-tailed point-spread functions *Proc. SPIE* 1092 17–21

Seeley G W, Borgstrom M C and Mazzeo J 1982 A general interactive computer program for running signal detection experiments *Behav. Res. Methods Instrum.* **4** 555–6

Seibert J A and Boone J M X-ray scatter removal by deconvolution 1988 *Med. Phys.* **15** 567–75

Swets J A 1979 ROC analysis applied to the evaluation of medical imaging techniques *Invest Radiol.* **14** 109–21

Swets J A and Pickett R M 1982 *Evaluation of Diagnostic Systems* (New York: Academic)

Tanner W P and Birdsall T G 1958 Definition of d' and η as psychophysical measures *J. Acoust. Soc. Am.* **30** 922–8

Tsui B M W, Metz C E, Atkiss F B, Starr S J and Beck R N 1977 A comparison of optimum detector spatial resolution in nuclear imaging based on statistical theory and on observer performance *Phys. Med. Biol.* **23** 654

Van Trees H L 1968 *Detection, Estimation and Modulation Theory* vols I–III (New York: Wiley)

Wagner R F, and Brown D G 1982 Overview of a unified SNR analysis of medical imaging systems *IEEE Trans. Med. Imag.* **MI-1** 210–14

—— 1985 Unified SNR analysis of medical imaging systems *Phys. Med. Biol.* **30** 489–518

Watson A B, Barlow H B and Robson J G 1983 What does the eye see best? *Nature* **302** 419–22

Whalen A D 1971 *Detection of Signals in Noise* (New York: Academic)

Yanch J C, Irvine A T, Webb S and Flower M A 1988 Deconvolution of emission tomographic data: a clinical evaluation *Br. J. Radiol.* **61** 221–5